Constraining the axion mass through gamma-ray observations of pulsars

Sheridan J. Lloyd[*], Paula M. Chadwick,[†] and Anthony M. Brown[‡]

Centre for Advanced Instrumentation, Dept. of Physics, University of Durham,
South Road, Durham DH1 3LE, United Kingdom

We analyze nine years of PASS 8 *Fermi*-LAT data in the 60–500 MeV range and determine flux upper limits (ULs) for 17 gamma-ray dark pulsars as a probe of axions produced by nucleon-nucleon Bremsstrahlung in the pulsar core. Using a previously published axion decay gamma-ray photon flux model for pulsars which relies on a high core temperature of 20 MeV, we improve the determination of the UL axion mass (m_a), at 95% confidence level, to 9.6×10^{-3} eV, which is a factor of 8 improvement on previous results. We show that the axion emissivity (energy loss rate per volume) at realistic lower pulsar core temperatures of 4 MeV or less is reduced to such an extent that axion emissivity and the gamma-ray signal becomes negligible. We consider an alternative emission model based on energy loss rate per mass to allow m_a to be constrained with *Fermi*-LAT observations. This model yields a plausible UL m_a of 10^{-6} eV for pulsar core temperature less than 0.1 MeV, but knowledge of the extent of axion-to-photon conversion in the pulsar B field would be required to make a precise UL axion mass determination. The peak of the axion flux is likely to produce gamma rays in the less than 1 MeV energy range, and so future observations with medium-energy gamma-ray missions, such as AMEGO and e-ASTROGAM, will be vital to further constrain UL m_a.

I. INTRODUCTION

The axion, a Nambu-Goldstone boson, is a solution to the strong *CP* problem of QCD and a plausible cold dark matter candidate [1–3]. The mass of the axion m_a can be constrained by astrophysical arguments such as the duration of the neutrino burst of SN-1987A ($m_a < 5 \times 10^{-3}$ eV) [4] or by direct detection experiments such as ADMX [5] where Galactic halo axions convert to microwave photons in a magnetic field, excluding m_a in the range $(1.9–3.53) \times 10^{-6}$ eV [6–10]. The authors of Ref. [11] have used cooling simulations, combined with surface temperature measurements of four thermal x-ray emitting pulsars (PSRs), to determine $m_a < (0.06–0.12$ eV$)$. In the gamma-ray regime, the authors of Ref. [12] have used five years of PASS 7 *Fermi*-LAT gamma-ray observations of radiative axion decay in four nearby PSRs to constrain $m_a < 0.079$ eV.

The latest data release of the *Fermi*-LAT is now PASS 8, which incorporates improvements to further reduce gamma-ray background uncertainty, improve the instrument effective area and point spread function (PSF), and permit low-energy analysis down to 60 MeV. In this paper, we will seek to refine the work of Ref. [12] to take advantage of the improved low-energy analysis in PASS 8,

coupled with improved photon statistics (nine years of event data) and a larger sample of 17 gamma-ray dark PSRs. This should allow a more robust determination of UL m_a than was possible previously.

This paper is structured as follows. In Sec. II, we describe the phenomenology of the axion and its production in neutron stars. In Sec. III, we describe the criteria used to select pulsars for analysis. In Sec. IV, we describe our analysis method for the determination of gamma-ray upper limits from the pulsar sample. In Sec. V, we present UL energy and photon flux determinations for the pulsar sample and from these derive the axion mass upper limit m_a by two independent methods. In Sec. VI, we discuss the validity of the UL m_a determination with respect to the pulsar core temperature. Finally, in Sec. VII, we summarize our findings and make suggestions for future work.

II. PHENOMENOLOGY

In this section, we discuss the mechanism for axion production in degenerate pulsar cores and describe how this process is modeled through a spin structure function. We then restate how the axion emissivity or energy loss rate per volume is expressed in terms of this spin structure function. We use a published astrophysical model for the photon flux arising from axion emission and decay in pulsars to derive an expression for UL axion mass. Finally, we derive an alternative expression for UL axion mass by using the

[*]sheridan.j.lloyd@durham.ac.uk
[†]p.m.chadwick@durham.ac.uk
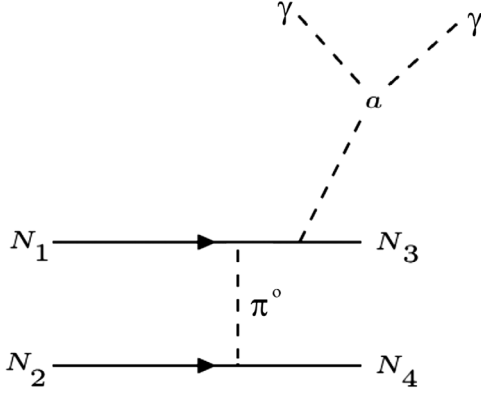[‡]anthony.brown@durham.ac.uk

FIG. 1. Feynman diagram depicting the nucleon-nucleon Bremsstrahlung process which produces axions. Incoming nucleons $N_{1,2}$ undergo a one-pion exchange, producing an axion a and outgoing nucleons $N_{3,4}$ with different energy and momenta than those of $N_{1,2}$. The axion undergoes radiative (conservative) decay to two gamma-ray photons.

expected energy loss rate per mass due to axion production to give an expected gamma-ray luminosity for a canonical pulsar and then equate this to the measured gamma-ray upper limits of the pulsars we consider.

Axions may be produced in pulsar cores through the process of nucleon-nucleon Bremsstrahlung as depicted in the Feynman diagram of Fig. 1. The Bremsstrahlung process assumes a one-pion exchange (OPE) approximation [13], and the nucleons involved are considered to be neutrons. Incoming nucleons N_1, N_2 and outgoing nucleons N_3, N_4 undergo one-pion exchange to produce axions of energy ω via the Bremsstrahlung process. The axions then undergo radiative decay to gamma-ray photons.

The axion has a mass m_a, which is related to the Peccei-Quinn scale f_a through a scaling relation [Eq. (1)]:

$$m_a \approx 6\mu \text{ eV} \left(\frac{f_a}{10^{12} \text{ GeV}} \right)^{-1}. \qquad (1)$$

The spin structure function $S_\sigma(\omega)$ [Eq. (2)] is a phase space integral corresponding to the Bremsstrahlung process depicted in Fig. 1. The phase space integral accounts for nucleon spin and the balanced energy ($E_{1,2,3,4}$) and momenta ($\mathbf{p_{1,2,3,4}}$) transfer between nucleons $N_{1,2,3,4}$ with the conservation of momenta and energy provided by Dirac δ functions. The momenta $\boldsymbol{p}_i$ have integration limits in the range $0 < \boldsymbol{p}_i < 2p_{Fn}$, where p_{Fn} is the neutron *Fermi* momentum. p_{Fn} is 300–400 MeV in supernovae cores [14] and typically greater than 100 MeV in neutron stars [15]. $\mathcal{F}$ in Eq. (2) is the product of thermodynamic functions as defined in Eq. (3). $\mathcal{H}_{ij}$ is the hadronic tensor incorporating nucleon spin with value $10/\omega^2$. The rate of axion production can be determined independently of the OPE approximation using the soft-neutrino radiation rate, which is proportional to the nucleon nucleon on-shell scattering

amplitude. This soft-neutrino approximation (SNA) method gives an axion emission rate which is a factor of 4 smaller than that given by the OPE approximation [15]. It can be shown that a value of $\mathcal{H}_{ij} = 10/\omega^2$ largely includes the reduction in the axion emission rate expected for the SNA by considering expressions for the scattering kernel of neutrinos produced by Bremsstrahlung in supernovae cores as presented in Ref. [16] in which the SNA has not been applied. We can take the spin structure function $S_\sigma(\omega)$ [Eq. (2)] to be analogous to the neutrino scattering kernel $S_\sigma(\omega)$ of Ref. [16] and thus equate $\mathcal{H}_{ij}$ to the spatial trace, $\bar{M}$, in the neutrino scattering kernel expression of Ref. [16]. By combining the expressions presented in Ref. [16] for a generic scattering kernel, the spin fluctuation rate, and an effective degeneracy parameter, we obtain a $\mathcal{H}_{ij}$ value of $30/\omega^2$. Thus, a value of $10/\omega^2$ for $\mathcal{H}_{ij}$ results in a factor of 3 reduction in axion emissivity, which is comparable with the factor of 4 reduction expected from the SNA. The thermodynamic function [Eq. (4)] is the *Fermi*-Dirac distribution in natural units ($k_B = 1$) for the nucleons applicable to degenerate matter [17] incorporating energy E, temperature T, and neutron star degeneracy μ. We take the value of $\mu/T = 10$ as used in the analysis of Ref. [12]:

$$S_\sigma(\omega) = \frac{1}{4} \int \left[\prod_{i=1\ldots4} \frac{d^3 p_i}{(2\pi)^3} \right]$$
$$\times (2\pi)^4 \delta^3(\mathbf{p_1} + \mathbf{p_2} - \mathbf{p_3} - \mathbf{p_4})$$
$$\times \delta(E_1 + E_2 - E_3 - E_4 - \omega)\mathcal{F}\mathcal{H}_{ij} \qquad (2)$$

$$\mathcal{F} = f(E_1)f(E_2)(1 - f(E_3)(1 - f(E_4)) \qquad (3)$$

$$f(E) = 1/(1 + \exp((E - \mu)/T)). \qquad (4)$$

The axion emissivity or energy loss rate per volume in natural units (i.e., $\hbar = c = 1$), ϵ_a, is defined by Eq. (5) as given in Ref. [15], in which M_N is the nucleon mass of 938 MeV and g_{ann} is the axion-nucleon coupling with $g_{ann} = C_N M_N / f_a$. C_N encapsulates the vacuum expectation values for the Higgs u and d doublets with the doublets giving mass to the up and down quarks of the nucleons. The value of C_N depends on the coupling model considered with $0 < C_N < 2.93$ [18]; we take $C_N = 0.1$ as [12]

$$\epsilon_a = \frac{g_{ann}^2}{48\pi^2 M_N^2} \int \omega^4 S_\sigma(\omega) d\omega. \qquad (5)$$

The expected photon flux arising from axion decay for a photon of energy E is given by Eq. (6) from Ref. [12], in which d is the distance to the pulsar in parsecs and Δt is the timescale for the emission of axions from a neutron star with a core temperature of 20 MeV [Eq. (7)]. We take the value of $S_\sigma(\omega)$ to be 2.4×10^7 and 6.25×10^4 MeV^2 for axion energies of 100 and 200 MeV respectively from the

values of $\omega^4 S_\sigma(\omega)$ in the axion emissivity vs energy plot of Ref. [12] for a pulsar of core temperature 20 MeV and $\mu/T = 10$. We choose $S_\sigma(\omega)$ at $\omega = 100$ MeV and $\omega = 200$ MeV in our calculations because these represent reasonable extremes on the emissivity plot, with emissivity peaking and being less sensitive to energy near $\omega = 100$ MeV and an emissivity cutoff at $\omega = 230$ MeV,

$$E\frac{d\Phi}{dE} = 1.8 \times 10^{-2} \left(\frac{m_a}{\text{eV}}\right)^5 \left(\frac{\Delta t}{23.2\ \text{s}}\right) \left(\frac{100\ \text{pc}}{d}\right)^2$$
$$\times \left(\frac{2E}{100\ \text{MeV}}\right)^4 \left(\frac{S_\sigma(2E)}{10^7\ \text{MeV}^2}\right)\ \text{cm}^{-2}\ \text{s}^{-1} \quad (6)$$

$$\Delta t = 23.2 s \left(\frac{\text{eV}}{m_a}\right)^2. \quad (7)$$

By combining Eqs. (6) and (7), the UL axion mass can be expressed in terms of the UL gamma-ray photon flux Φ of a pulsar [Eq. (8)]:

$$\text{UL}\ m_a = \left[\text{UL}\ \Phi\ \text{cm}^{-2}\ \text{s}^{-1} \times 55.5 \times \left(\frac{d}{100\ \text{pc}}\right)^2\right.$$
$$\left.\times \left(\frac{100\ \text{MeV}}{2E}\right)^4 \left(\frac{10^7\ \text{MeV}^2}{S_\sigma(2E)}\right)\right]^{\frac{1}{3}}. \quad (8)$$

Alternatively, instead of using photon flux methods as described above, axion mass can be constrained using an expression for the energy lost from the pulsar as a result of axion production. The energy loss rate $\epsilon_a{}^D$ for a given mass of neutron star material arising from the production of axions in the pulsar core [Eq. (9)] is as presented in Ref. [19] based on Refs. [13] and [17] with α_a as Eq. (10). T_{MeV} is the neutron star core temperature in mega-electron-volts, and ρ_{15} is the neutron star mass density in units of $10^{15}\ \text{g cm}^{-3}$. We include a further factor of 0.25 in Eq. (9) to allow for the SNA reduction in axion emission rate,

$$\epsilon_a{}^D = 0.25 \times \alpha_a 1.74 \times 10^{31}\ \text{erg g}^{-1}\ \text{s}^{-1} \rho_{15}^{-2/3} T_{\text{MeV}}^6 \quad (9)$$

$$\alpha_a \equiv \left(\frac{C_N M_N}{f_a}\right)^2 / 4\pi. \quad (10)$$

The measured UL gamma-ray luminosity, L_γ, can be equated to the expected gamma-ray luminosity arising from the axion energy loss rate for the total mass of the neutron star as $L_\gamma = \epsilon_a{}^D NS_{\text{mass}} P_{a\to\gamma}$, where NS_{mass} is the neutron star mass expressed in grams and $P_{a\to\gamma}$ is the axion-to-photon conversion probability (0–1.0) in the pulsar B field. In the case of axion radiative decay where an axion decays to two gamma-ray photons, without conversion in the pulsar B field being required, we take $P_{a\to\gamma}$ to be $1.1 \times 10^{-24}\ \text{s}^{-1}\ (m_a/1\ \text{eV})^5$ [20]. From the above expression for L_γ and by combining Eqs. (1), (9), and (10), we obtain an expression for UL m_a [Eq. (11)]. We assume a canonical pulsar mass of 1.4 $M_\odot$ or 2.786×10^{33} g and a density of $0.056 \times 10^{15}\ \text{g cm}^{-3}$

$$\text{UL}\ m_a = \frac{6.0 \times 10^{15}}{C_N M_N} \left(\frac{4\pi L_\gamma\ \text{erg s}^{-1}}{0.435 \times 10^{31}\ \text{erg g}^{-1}\ \text{s}^{-1} \rho_{15}^{-2/3} T_{\text{MeV}}^6 NS_{\text{mass}} P_{a\to\gamma}}\right)^{\frac{1}{2}}. \quad (11)$$

III. PULSAR SELECTION

We make the simple assumption that axions are emitted in a continuous isotropic fashion by the pulsar and are unaffected by pulsar rotation. In making our pulsar selection, we want to maximize the probability of detecting isotropic gamma-ray emission arising solely from the decay of axions to gamma rays. Thus, we wish to exclude the pulsed gamma-ray emission arising from pulsar magnetospheric emission, which would be unrelated to axion production and a background to the axion signal that we wish to measure. Therefore, our selection of 17 pulsars (Table I) from version 1.57 of the Australia Telescope National Facility (ATNF) catalogue [21][1] is based on the following criteria to minimize gamma-ray background and to select well-measured pulsars which are most likely to emit detectable gamma rays solely through axion decay:

(i) We include pulsars which are located off the Galactic plane ($|b| > 15°$), thus reducing the uncertainty arising from the Galactic gamma-ray background model of the Galactic disk.

(ii) We include pulsars away from the Galactic Center with $l > 30°$ and $l < 330°$.

(iii) We include nearby pulsars with a heliocentric distance of 0.5 kpc or less and possessing an $\dot{E} > 0$ in the ATNF catalogue.

(iv) We include only pulsars which are not known to have binary companions in the ATNF catalogue and have not been identified as prior sources of gamma-ray emission in either the Public List of LAT-Detected Gamma-Ray Pulsars[2] (which lists all publicly announced gamma-ray pulsar detections,

---

[1]http://www.atnf.csiro.au/research/pulsar/psrcat/.

[2]https://confluence.slac.stanford.edu/display/GLAMCOG/Public+List+of+LAT-Detected+Gamma-Ray+Pulsars, list last updated October 19, 2018 (accessed on February 14, 2019).

TABLE I. Our selection of 17 pulsars from the ATNF catalogue showing their Galactic longitude/latitude, right ascension (RA) and declination (Dec) coordinates, period, pulsar distance, magnetic field B at surface and light cylinder in Gauss, $\dot{E}$, and spin-down age. Discovery and period are from the references listed.

Name and Ref.		l (deg)	b (deg)	RA (deg)	Dec (deg)	Period (s) and Ref.		Distance (kpc)	B surface (10^{10} Gauss)	B light cylinder (Gauss)	$\dot{E}$ (10^{30} erg s^{-1})	Spin-down age (10^5 Yr)
J0736−6304	[23]	274.88	−19.15	114.08	−63.07	4.863	[24]	0.10	2750.00	2.24	52.1	5.07
J0711−6830	[25]	279.53	−23.28	107.98	−68.51	0.005	[26]	0.11	0.03	16400	3550	58400
J0536−7543	[27]	287.16	−30.82	84.13	−75.73	1.246	[28]	0.14	84.90	4.12	11.5	349
J0459−0210	[29]	201.44	−25.68	74.97	−2.17	1.133	[30]	0.16	127.00	8.21	37.9	128
J0837+0610	[31]	219.72	26.27	129.27	6.17	1.274	[30]	0.19	298.00	13.50	130.0	29.7
J0108−1431	[32]	140.93	−76.82	17.03	−14.53	0.808	[30]	0.21	25.20	4.49	5.8	1660
J0953+0755	[31]	228.91	43.70	148.29	7.93	0.253	[30]	0.26	24.40	141.00	560.0	175
J1116−4122	[27]	284.45	18.07	169.18	−41.38	0.943	[33]	0.28	277.00	31.00	374.0	18.8
J0630−2834	[34]	236.95	−16.76	97.71	−28.58	1.244	[30]	0.32	301.00	14.70	146.0	27.7
J0826+2637	[35]	196.96	31.74	126.71	26.62	0.531	[30]	0.32	96.40	60.50	452.0	49.2
J1136+1551	[31]	241.90	69.20	174.01	15.85	1.188	[30]	0.35	213.00	11.90	87.9	50.4
J0656−5449	[36]	264.80	−21.14	104.20	−54.82	0.183	[36]	0.37	7.74	118.00	205.0	909
J0709−5923	[36]	270.03	−20.90	107.39	−59.40	0.485	[36]	0.37	25.00	20.50	43.5	610
J0636−4549	[37]	254.55	−21.55	99.14	−45.83	1.985	[37]	0.38	254.00	3.05	16.0	99.1
J0452−1759	[38]	217.08	−34.09	73.14	−17.99	0.549	[30]	0.40	180.00	102.00	1370.0	15.1
J0814+7429	[39]	140.00	31.62	123.75	74.48	1.292	[30]	0.43	47.20	2.05	3.1	1220
J2307+2225	[40]	93.57	−34.46	346.92	22.43	0.536	[41]	0.49	6.91	4.21	2.2	9760

the significance of which exceeds 4σ) or in the Second *Fermi* Large Area Telescope Catalog of Gamma-Ray Pulsars [22].

IV. ANALYSIS

A. Photon event data selection

The data in this analysis were collected by *Fermi*-LAT between August 4, 2008 to October 18, 2017 (Mission Elapsed Time 2395574147 to 530067438 s). We consider all PASS 8 events which are *source* class photons (evclass = 128), with Front converting events (evtype = 1), spanning the energy range 60 to 500 MeV. We use Front[3] converting events because of the improved PSF of this event class with 95% containment of 60 MeV photons at a containment angle of 13° as opposed to 20° for both Front and Back converting events. We select a conservative energy range of 60–500 MeV, as axion decay has previously been expected to produce gamma rays in the range 60–200 MeV, with a cutoff by 200 MeV [12]. Throughout our analysis, the *Fermipy* software package[4] [42] with version V10R0P5 of the *Fermi Science Tools* is used, in conjunction with the P8R2_SOURCE_V6 instrument

response functions. We apply the standard PASS 8 cuts to the data, including a zenith angle 90° cut to exclude photons from the Earth limb and good-time-interval cuts of DATA_QUAL > 0 and LAT_CONFIG = 1. The energy binning used is four bins per decade in energy, and spatial binning is 0.1° per image pixel.

B. Determining if pulsars are gamma-ray emitters

We first determine if any of the pulsars in our selection are significant unpulsed gamma-ray emitters. For each pulsar, we consider a 20° radius of interest (ROI) centered on the pulsar coordinates. We use a ROI of 20°, as our analysis is made down to a low energy of 60 MeV and we wish to be certain to allow for the contribution of low-energy sources given the PSF of 13° above.

We include known sources using a point source population derived from the *Fermi*-LAT's third point source catalog (3FGL), diffuse gamma-ray emission, and extended gamma-ray sources. The diffuse gamma-ray emission consists of two components: the Galactic diffuse flux and the isotropic diffuse flux. The Galactic component is modeled with *Fermi*-LAT's gll_iem_v06.fits spatial map with the normalization free to vary. The isotropic diffuse emission is defined by *Fermi's* iso_P8R2_SOURCE_V6_FRONT_v06.txt tabulated spectral data. The normalization of the isotropic emission is also left free to vary. In addition, all known sources take their spectral shape as defined in the 3FGL catalog.

An energy dispersion correction is applied to the pulsar test source but disabled for all 3FGL sources, in line with

---

[3] We have repeated the same analysis using the PSF3 event class, which is the best quartile direction reconstruction. This does not change the determined m_a significantly considering all 17 PSRs. We therefore retain the Front analysis to allow direct comparison with Ref. [12].

[4] *Fermipy* change log version 0.12.0.

Fermi Science Support Centre recommendations for low-energy analysis.

We perform an initial BINNED likelihood analysis using the OPTIMIZE method with the normalization of all point sources within 20° of the pulsar being left free.

From this initial likelihood fit, all point sources (with the exception of the target pulsar) with a test statistic (TS) less than 4, or with a predicted number of photons, Npred < 4, are removed from the model. Thereafter, we free the spectral shape of all sources with TS greater than 25 in this refined model and undertake a further secondary likelihood fit using the OPTIMIZE and FIT methods.

The best-fit model from this secondary likelihood fit is then used with the *Fermi Science Tool* GTTSMAP, to search for new point sources that were not already present in the 3FGL. In particular, we run *Fermipy*'s FIND_SOURCES method to detect all sources above 3σ significance. FIND_SOURCES is a peak detection algorithm which analyzes the TS map to find new sources over and above those defined in the 3FGL model by placing a test point source, defined as a power law with spectral index 2.0, at each pixel on the TS map and recomputing likelihood. Lastly, we again run the FIT method to perform a final likelihood fit, which fits all parameters that are currently free in the model and updates the TS and predicted count (Npred) values of all sources.

C. Pulsar upper limit gamma-ray emission

In order to determine PSR gamma-ray flux upper limits, we repeat the analysis of Sec. IV B with a source model which includes a pulsar test source for each of the 17 pulsars. The differential flux, dN/dE, (photon flux per energy bin) of the test source for each pulsar is described as a power law[5] as defined in Eq. (12) where prefactor $= N_0$, index $= \gamma$, and scale $= E_0$. The test source has an index of 2.0, a scale of 1 GeV, and a prefactor of 1×10^{-11}. We leave the prefactor (normalization) and index of the test source free to vary,

$$\frac{dN}{dE} = N_0 \left(\frac{E}{E_0}\right)^{\gamma}. \tag{12}$$

We then obtain UL photon and energy fluxes integrated over the energy analysis range (at 2σ significance, 95% confidence level) from the FLUX_UL95 and EFLUX_UL95 attributes respectively of the *Fermipy* sources entry for each pulsar test source. The UL photon and energy fluxes are defined as the values where the likelihood function, 2ΔLog(L), which compares the likelihood of a model with the source and without, has decreased by 2.71 from its maximum value across the range of flux values arising from the analysis. In addition, we use a composite likelihood stacking technique to improve the UL photon flux

---

[5]As described in the *Fermi* Science Support Centre link https://fermi.gsfc.nasa.gov/ssc/data/analysis/scitools/source_models.html.

determination by considering all test sources in the analysis together. We extract a likelihood profile of ΔLog(L) vs the photon flux for each test source using the *Fermipy* PROFILE_NORM method. Next, we determine the functional form of this likelihood profile for each test source using numpy polyfit and poly1d and interpolate the likelihood profile with numpy polyval between the overall minimum and maximum photon flux values obtained by considering the UL photon flux of all test sources. We then sum the ΔLog(L) values of each interpolated likelihood profile to obtain a single stacked ΔLog(L) vs photon flux profile for the test sources as a whole. Finally, we determine the maximum photon flux where the stacked ΔLog(L) has decreased by 1.35 from its peak value to give the one-sided upper limit photon flux.

V. RESULTS

A. Pulsar UL gamma-ray fluxes

We list the UL photon, energy fluxes, and gamma-ray luminosities (assuming the distances in Table I) for our sample of pulsars in Tables II and III. The UL photon flux at 95% confidence obtained by likelihood stacking of all 17 pulsars is 7.8×10^{-10} cm^{-2} s^{-1}.

B. Upper limit m_a determination

We list our determination of UL m_a in Tables II and III for each pulsar derived from the UL photon flux and Eq. (8) for axions of energy 100 and 200 MeV. The average UL m_a considering all 17 pulsars is 9.6×10^{-3} eV and 3.21×10^{-2} eV for axions of energy 100 and 200 MeV respectively. We obtain an average UL m_a for the four pulsars analyzed in [12], J0108 $-$ 1431, J0953 $+$ 0755, J0630$-$2834, and J1136 $+$ 1551 of 9.8×10^{-3} eV and 3.29×10^{-2} eV for axions of energy 100 and 200 MeV respectively.

Our determination of UL $m_a = 9.6 \times 10^{-3}$ eV is a factor of 8 improvement on the result of Ref. [12], in which an UL m_a of 7.9×10^{-2} eV was determined.

Finally, we note that the UL m_a obtained by likelihood stacking is improved twofold compared to the averaged result above, with an UL m_a of 4.8×10^{-3} eV and 1.61×10^{-2} eV for axions of energy 100 and 200 MeV respectively.

C. Pulsars near extended emission

We note that the UL test sources for five pulsars are detected with a significance which exceeds 3σ, namely J0736 $-$ 6304 5.7σ (TS 33), J0630 $-$ 2834 4.4σ (TS 19), J2307 $+$ 2225 3.7σ (TS 14), J0709 $-$ 5923 3.5σ (TS 12), and J0459 $-$ 0210 3.2σ (TS 10). However, the initial analysis which searches for point sources (while not introducing a pulsar test source) detects no point sources at the pulsar coordinates, and thus we discount these

TABLE II.   Test statistic, UL photon flux, UL energy flux, UL gamma luminosity, and UL m_a for axion energies of 100 and 200 MeV for the 12 undetected pulsars.

Pulsar	TS	UL photon flux $(10^{-8}\ \mathrm{cm}^{-2}\,\mathrm{s}^{-1})$	UL energy flux $(10^{-12}\ \mathrm{erg}\,\mathrm{cm}^{-2}\,\mathrm{s}^{-1})$	UL γ luminosity $(10^{31}\ \mathrm{erg}\,\mathrm{s}^{-1})$	UL m_a $\omega = 100$ MeV $(10^{-2}\ \mathrm{eV})$	UL m_a $\omega = 200$ MeV $(10^{-2}\ \mathrm{eV})$
$J0711 - 6830$	3	0.04	1.51	0.22	0.21	0.70
$J0536 - 7543$	0	0.22	0.53	0.12	0.43	1.45
$J0837 + 0610$	0	0.27	0.63	0.27	0.57	1.90
$J0108 - 1431$	0	0.18	0.41	0.21	0.52	1.75
$J0953 + 0755$	2	0.47	1.32	1.07	0.84	2.81
$J1116 - 4122$	1	0.90	1.73	1.62	1.09	3.66
$J0826 + 2637$	2	0.39	1.18	1.44	0.91	3.04
$J1136 + 1551$	0	0.50	1.16	1.70	1.04	3.49
$J0656 - 5449$	0	0.32	0.75	1.23	0.94	3.14
$J0636 - 4549$	3	1.31	2.08	3.60	1.52	5.08
$J0452 - 1759$	0	0.31	0.71	1.36	0.97	3.24
$J0814 + 7429$	0	0.23	0.54	1.19	0.93	3.10

TABLE III.   Test statistic, UL photon flux, UL energy flux, UL gamma luminosity, and UL m_a for axion energies of 100 and 200 MeV for the five pulsars which are associated with areas of extended diffuse gamma-ray emission.

Pulsar	TS	UL photon flux $(10^{-8}\ \mathrm{cm}^{-2}\,\mathrm{s}^{-1})$	UL energy flux $(10^{-12}\ \mathrm{erg}\,\mathrm{cm}^{-2}\,\mathrm{s}^{-1})$	UL γ luminosity $(10^{31}\ \mathrm{erg}\,\mathrm{s}^{-1})$	UL m_a $\omega = 100$ MeV $(10^{-2}\ \mathrm{eV})$	UL m_a $\omega = 200$ MeV $(10^{-2}\ \mathrm{eV})$
$J0736 - 6304$	33	2.68	4.87	0.58	0.79	2.65
$J0459 - 0210$	10	1.72	3.64	1.11	0.93	3.13
$J0630 - 2834$	19	1.89	3.59	4.40	1.53	5.12
$J0709 - 5923$	12	1.03	2.55	4.17	1.38	4.62
$J2307 + 2225$	14	1.12	2.87	8.25	1.71	5.72

apparent detections as true detections of the pulsars concerned. The lack of significant point source pulsar detections can also be seen on TS maps for the analysis (Fig. 2) where the pulsars are spatially coincident with regions of extended gamma-ray emission uncharacteristic of the point source emission expected from a pulsar.

We also check for source extension of the pulsars by running the GTANALYSIS EXTENSION method. EXTENSION replaces the pulsar point source spatial model with an azimuthally symmetric two-dimensional Gaussian model. It then profiles the likelihood with respect to spatial extension in a one-dimensional scan to determine the likelihood of extension. Only the J0736-6304 test source has some evidence of extension with an extension TS value of 14 (3.7σ). The remaining four pulsars with significance less than 4.4σ are consistent with background and as expected have no significant extension.

We make the assumption that axion emission is isotropic, and so the extended emission of J0736-6304, which is asymmetric and exhibits its highest significance offset from the pulsar, would seem to be inconsistent with an axion source. Instead, this emission is more likely to be consistent with variations in the Galactic diffuse gamma-ray background.

These five pulsars generally exhibit higher UL fluxes (Table III) than the other 12 (Table II), and so omitting these

five pulsars from the determination of UL m_a yields an improved average UL m_a for the 12 remaining pulsars of 8.9×10^{-3} eV and 2.97×10^{-2} eV for axions of energy 100 and 200 MeV respectively.

VI. DISCUSSION

A. Upper limit determination

The authors of Ref. [12] analyzed four pulsars, $J0108 - 431$, $J0953 + 0755$, $J0630 - 2834$, and $J1136 + 1551$, with an UNBINNED likelihood analysis using the 2FGL catalog, with five years of *Fermi*-LAT PASS 7 event data in the energy range 60–200 MeV, and employing front converting source photon events. They detected no gamma-ray emission and determined a 95% confidence UL photon flux for each of the four pulsars using the MINOS method of the *Fermi Science Tools*. In contrast, we analyze 17 pulsars (including the four pulsars of Ref. [12]) with a BINNED likelihood analysis using the 3FGL catalog and nine years of *Fermi*-LAT PASS 8 event data in the energy range 60–500 MeV, again using front converting events. We determine the UL photon flux using the *Fermipy* FLUX_UL95 entry for each pulsar. Using this analysis, we obtain UL photon fluxes (Table V) comparable to Ref. [12] for the
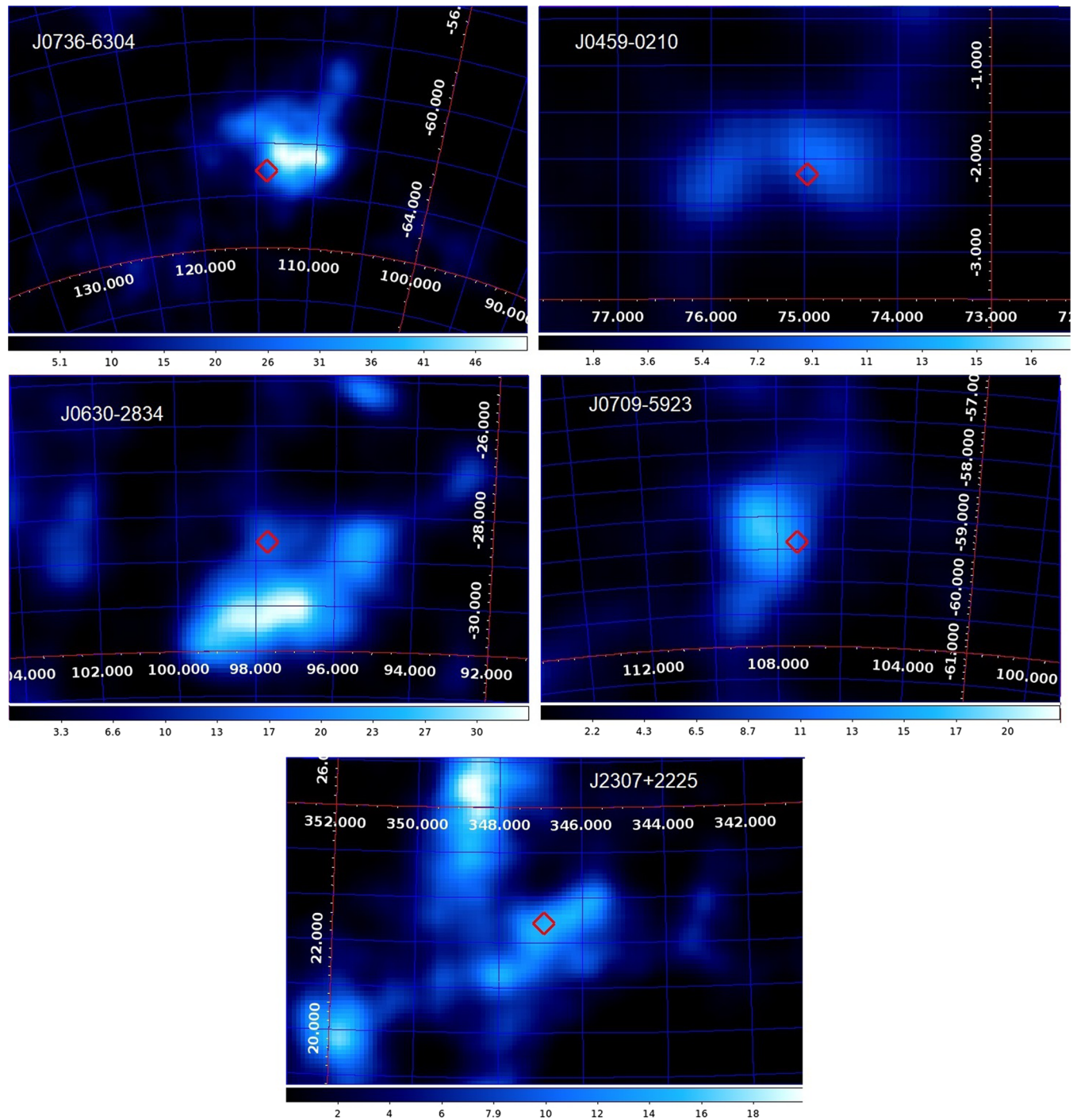
FIG. 2.   TS maps for our gamma-ray analysis of the five pulsar test sources detected at greater than 3σ significance (Table III) showing that these sources are inconsistent with a point source detection characteristic of pulsars and part of extended diffuse features. The horizontal contour scale is the TS value, the red diamond is the pulsar position, the horizontal axis is RA in decimal degrees, and the vertical axis is Dec in decimal degrees.

four pulsars they consider, which serves as a useful check of our gamma-ray analysis method, and do not detect any pulsars in our sample.

Our method to determine UL m_a differs from Ref. [12] in that we use UL photon fluxes directly as input to Eq. (8), while they fit a model of the spectral energy distribution

(SED) of differential flux to a stacked likelihood analysis of the four pulsars using the COMPOSITE2 module of the *Fermi Science Tools* and take the UL normalization of this model to be UL $(m_a/\text{eV})^5$ from which they obtain UL m_a with all flux dependencies on astrophysical factors being accounted for in the SED model.

TABLE IV. Definition of the FILEFUNCTION spectral model with differential flux at a given energy.

Energy (MeV)	Differential flux ($cm^{-2} s^{-1} MeV^{-1}$)
50	2×10^{-3}
60	8×10^{-4}
70	4×10^{-4}
80	1×10^{-4}
90	6×10^{-5}
100	2×10^{-5}
200	1×10^{-11}

We can use the UL photon fluxes obtained by Ref. [12] to consider the improvement in UL m_a determination which arises from our UL m_a calculation method alone. The average UL m_a for the four pulsars using the Ref. [12] photon fluxes (Table V) and our method [Eq. (8)] is 9.7×10^{-3} and 3.25×10^{-2} eV for axions of energy 100 and 200 MeV, improving on the 7.9×10^{-2} eV determination of Ref. [12] by a factor of 2.4–8.1. Despite this improvement, we note that our determination of UL m_a is conservative because we assume that the integrated UL photon flux arises solely from a specific axion energy (100 or 200 MeV) rather than the lower UL flux (and hence more constraining) UL m_a determination which would be expected if we could determine UL photon flux for each energy bin in the analysis energy range of 60–500 MeV.

We determine a very similar UL m_a in our sample of 17 pulsars of 9.6×10^{-3} and 3.21×10^{-2} eV for axions of energies 100 and 200 MeV respectively. These results are also comparable with UL m_a values obtained by modeling the cooling of Cassiopeia A observed by *Chandra*. By assuming that the cooling results from both neutrino and axion emission and that a state of superfluidity exists in the star, an UL m_a of $(1.7–4.8) \times 10^{-2}$ eV is obtained for $C_N = (0.14 - -0.05)$ [43].

In a final check to test whether the SED differential flux model used by Ref. [12] can be fitted individually to any of our 17 pulsars, we add a test source with the SED differential flux model from Ref. [12] implemented using the FILEFUNCTION spectral model [Eq. (13)] with flux values as Table IV and reanalyze as Sec. IV above. All 17 pulsars remain undetected with the differential flux model

test source exhibiting a consistent normalization of 10^{-5} for all pulsars, which is equivalent to $m_a < 0.1$ eV,

$$\frac{dN}{dE} = N_0 \left(\frac{dN}{dE} \right) \Big|_{\text{file}}. \tag{13}$$

B. Effect of pulsar core temperature

The emission rate for axions is strongly dependent on pulsar core temperature, T_c, being proportional to T_c^6 [17]. We therefore reexamine the applicable value of T_c for modeling axion emission and the effect of lowering T_c on that emission. The authors of Ref. [12] select $T_c = 20$ MeV on the basis of the range temperatures applicable to equation of state (EOS) simulations of pulsar degenerate matter [44–46], slower neutron star cooling due to superfluidity [47,48], and surface temperature observations of the pulsar J0953 + 0755 [49].

We now consider to what extent the works cited above explicitly support the choice of $T_c = 20$ MeV. In EOS modeling, both Refs. [44] and [45] use T_c as a free model parameter (in the range 0–60 and 0–15 MeV respectively) for the construction of phase diagrams, but this does not indicate a preferential value for T_c. In Ref. [46], a specific *Fermi* temperature T_F of 20 MeV per nucleon is supported, but no preferred value of T_c is indicated. The cooling of quark hybrid (QH) stars (a special case of a higher density neutron star where quarks experience deconfinement from nucleons) is considered in Ref. [47] with QH stars in fact cooling *more* quickly than hadron neutron stars unless a color flavor locked (CFL) quark phase with a higher CFL gap parameter of 1 MeV is considered. However, by 10^5 years, all modeled QH stars again exhibit *greater* cooling than hadron neutron stars. As all neutron stars in our pulsar sample have an age greater than 10^5 years (Table I), this QH star slow cooling regime will not result in a higher value for T_c in our sample than might be expected from normal cooling processes. The discussion of crustal heating arising from super fluidity in neutron stars also refutes $T_c = 20$ MeV, with one neutron star J0953 + 0755 (PSR 0950 + 08) analyzed in Ref. [12] having an internal temperature of between 0.09 and 0.11 keV [48]. Although there is more recent evidence of internal heating of J0953 + 0755 from far

TABLE V. The UL photon flux for four pulsars from Ref. [12] (60–200 MeV) compared to our analysis (60–500 MeV) and UL m_a, which we derive from Ref. [12] fluxes for axions of energy 100 and 200 MeV using Eq. (8).

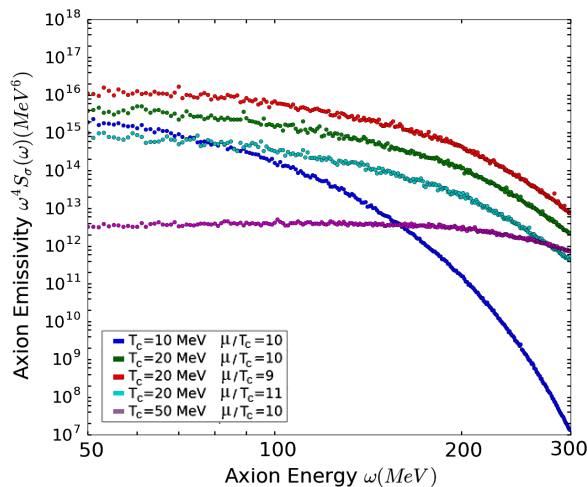| Pulsar	UL photon flux (60–200 MeV) (from Ref. [12]) (10^{-9} $cm^{-2} s^{-1}$)	UL photon flux (60–500 MeV) (this analysis) (10^{-9} $cm^{-2} s^{-1}$)	UL m_a $\omega = 100$ MeV (10^{-2} eV)	UL m_a $\omega = 200$ MeV (10^{-2} eV)
J0108 − 1431	4.03	1.75	0.69	2.31
J0953 + 0755	7.40	4.75	0.97	3.26
J0630 − 2834	4.82	18.90	0.97	3.25
J1136 + 1551	8.52	5.01	1.25	4.17

FIG. 3. The energy dependence of axion emissivity $\omega^4 S_\sigma(\omega)$ on axion energy ω for varying pulsar core temperature T_c and μ/T_c derived by Monte Carlo numerical integration of an analytic simplification of $S_\sigma(\omega)$.

UV Hubble Space Telescope observations (surface temperature (ST) $= (1–3) \times 10^5$ K [50] vs 7×10^4 K of Ref. [49]), this would still only result in a maximum T_c of 1.34 keV assuming $T_c = 12 \times (\text{ST}/10^6 \text{ K})^{1.82}$ keV, Refs. [48,51].

The authors of Ref. [52] have modeled the cooling of neutron stars using a fully general relativistic stellar evolution code, without exotic cooling, allowing for inputs for equations of state and uncertainties in superfluidity along with a finite timescale of thermal conduction. They determine T_c to be initially 3.98×10^9 K (343 keV) when the neutron star is nine hours old, decreasing to 1.99×10^9 K (171 keV) at 1 year, 6.31×10^8 K (54 keV) at 1000 years, and 1.99×10^8 K (17 keV) at 10^5 years. This cooling trend agrees well with the modeling of pulsar cooling in Ref. [53] where the highest pulsar surface temperatures (in all scenarios) of 3.98×10^6 K at 1 year and 1.99×10^6 K at 10^5 years yield a T_c of 148 and 12 keV respectively using the ST-to-T_c conversion above. It should also be noted that *Chandra* observations of the very young pulsar Cas A (age approximately 330 years) yield a ST of 2.04×10^6 K [54], equivalent to $T_c = 43.9$ keV using the ST-to-T_c conversion above. Similarly, in modeling Cas A cooling using the observations of Ref. [54], the author of Ref. [43] determines the T_c of Cas A to be 7.2×10^8 K, equivalent to 62 keV.

We therefore consider $T_c = 20$ MeV to be a high temperature choice more consistent with the neutron star core just after the supernova event. In Ref. [55], EOS and hydrodynamic modeling is performed in the first second after the supernova core bounce and protoneutron star (PNS) creation. Here, at 150 ms post-bounce, T_c can be 14 MeV at the core, falling to 10 MeV at a radius of 10 km, before rising to a peak of 32 MeV at radius 12 km. Other modeling work demonstrates that a peak PNS T_c of 30

to 43 MeV is possible, falling to 5 to 18 MeV within 50 s [56] due to efficient cooling by neutrino emission. A very short time later, at 120 s, the PNS T_c is 2.2 MeV [57]. This suggests that plausible values of T_c are much less than 20 MeV, with $T_c = 1$ MeV being achieved within seconds [58].

We reevaluate $\omega^4 S_\sigma(\omega)$, on which the axion emissivity depends [Eq. (5)], for $T_c < 20$ MeV. We use the analytic simplification for the phase space integral for $S_\sigma(\omega)$ from Ref. [16] and perform a five-dimensional numeric Monte Carlo integration as described in the Appendix. In order to check our method, we first reproduce the $\omega^4 S_\sigma(\omega)$ plot from Ref. [12] using a T_c of 10–50 MeV, $\mu/T_c = 9$–11, and $p_{Fn} = 300$ MeV (Fig. 3).

We reproduce the essential features of the Ref. [12] plot both in magnitude and in the following respects:

  (i) Increasing the value of μ/T_c for fixed $T_c = 20$ MeV decreases the amplitude of $\omega^4 S_\sigma(\omega)$.

 (ii) $\omega^4 S_\sigma(\omega)$ for $T_c = 10$ MeV cuts off at a lower value of $\omega = 100$ MeV than for $T_c = 20$ MeV.

(iii) The $T_c = 50$ MeV case has lower values of $\omega^4 S_\sigma(\omega)$ than the $T_c = 20$ MeV case, with $\omega^4 S_\sigma(\omega)$ remaining broadly flat across higher ω values of 100–300 MeV with no pronounced cutoff at 200–300 MeV.

(iv) The value of $\omega^4 S_\sigma(\omega)$ spans one order of magnitude for the 20 MeV case whilst varying μ/T_c between 9 and 11.

We then evaluate $\omega^4 S_\sigma(\omega)$, in a lower temperature regime, for $p_{Fn} = 300$ MeV, $\mu/T_c = 10$ and consider lower pulsar core temperatures with $T_c = 1$–20 MeV (Fig. 4). Lowering T_c from 20 MeV to a plausible PNS temperature of 4 MeV reduces axion emissivity and hence gamma-ray emission by a factor of 10^8 for axions of energy $\omega = 100$ MeV. It therefore seems implausible that there would be detectable gamma-ray emission to allow the determination of m_a using the astrophysical model of gamma-ray emission from Ref. [12] [Eq. (6)], for realistic pulsar core temperatures. We note, however, that this model is based on a quite conservative assumption that gamma-ray emission arises solely from axion radiative decay as opposed to axion-to-gamma-ray photon conversion in the B field of the pulsar. It is therefore possible that an alternative model allowing axion-to-photon conversion could produce detectable gamma-ray emission.

The probable lack of detectable gamma-ray emission in the lower temperature regime leads us to derive values for UL m_a from an alternative model [Eq. (11)] based on the axion power equation which defines an energy loss rate due to axion production in the pulsar core [Eq. (9)]. Using the UL gamma-ray luminosity (Table II), we determine UL m_a from Eq. (11), while varying T_c and the probability of axion-to-photon conversion in the pulsar B field. In Fig. 5, we show the range of UL m_a values that we obtain. We see that the conversion of axions to gamma-ray photons via radiative decay results in the highest UL m_a (67.5 eV at
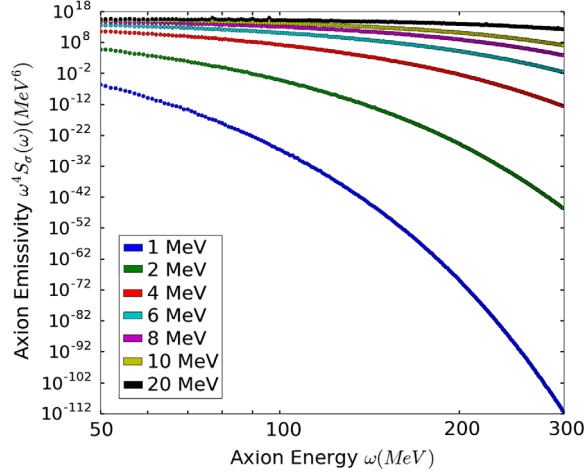
FIG. 4. The energy dependence of axion emissivity $\omega^4 S_\sigma(\omega)$ on axion energy ω for $T_c = 1–20$ MeV and $\mu/T_c = 10$ derived by Monte Carlo numerical integration of an analytic simplification of $S_\sigma(\omega)$. Reducing T_c from 20 to 4 MeV lowers emissivity by a factor of 10^8 at $\omega = 100$ MeV.

0.1 MeV, 9.4 eV at 1 MeV, and 0.7 eV at 20 MeV, points A, B, and C respectively), which is above the classic m_a search range of $10^{-2}–10^{-6}$ eV. Similarly, by varying the axion-to-photon conversion probability from 0.001 to 1.0 (total conversion), we only obtain an UL m_a above the lower search bound of 10^{-6} eV for $T_c < 0.1$ MeV independent of the degree of axion-to-photon conversion or $T_c < 0.4$ MeV assuming a probability of less than or equal to 0.001 for axion-to-photon conversion (points E and F of Fig. 5 respectively). At $T_c = 1$ keV, the lowest UL m_a obtainable would be 3.0 eV, assuming total conversion of axions to photons (point D of Fig. 5). We do not offer a view on the degree of axion-to-photon conversion in the pulsar B field but simply present a range of conversion alternatives to give indicative values of the UL m_a.

The determination of a plausible and precise UL m_a from this alternative model thus requires both realistic lower values of T_c and a knowledge of the precise extent of the axion-to-photon conversion in the pulsar B field. We have dealt with the value of T_c in the PNS and old pulsar cases above; however, while Ref. [12] considers there to be no axion-to-photon conversion in the pulsar B field (using vacuum birefringence arguments), there is no consensus on the extent of axion-to-gamma-ray photon conversion in pulsar B fields. More attention has been paid to axion-to-x-ray photon interconversion in pulsars [59] and in axion-like particles-to-x-ray conversion in the higher B field $(20 \times 10^{14}$ G) of magnetars by Ref. [60]. Reference [60] finds $P_{a\to\gamma} = 0.225$ for $\omega = 3$ keV (the peak emission) and $P_{a\to\gamma} = 0.025$ for $\omega = 200$ keV when $T_c = 50–250$ keV. The lower B field of our sample notwithstanding (average $B = 2.78 \times 10^{12}$ G) such values of $P_{a\to\gamma}$ and T_c could yield constraints on m_a in the classic axion search range using the alternative model (Fig. 5).
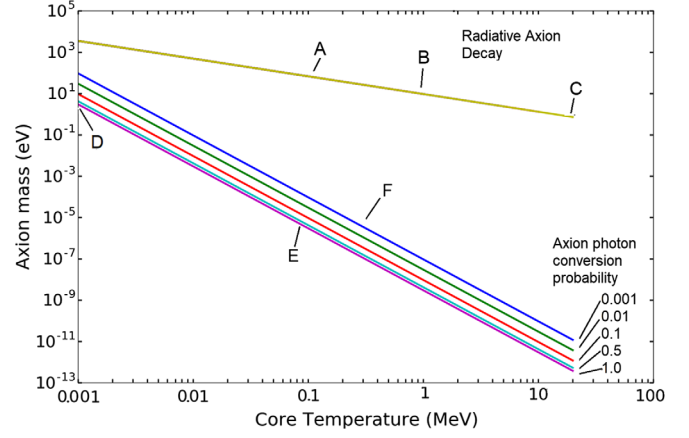

FIG. 5. Plot of axion mass with respect to T_c using an alternative energy loss rate model and varying axion-to-photon conversion probabilities from 0.001 to 1.00. Also shown is the more conservative axion radiative decay case (top). At realistic values of T_c of 0.1 and 1 MeV, radiative decay alone yields unrealistic values for UL m_a of 67.5 and 9.4 eV respectively (labeled A and B). At an unrealistic high value of 20 MeV for T_c, the UL m_a is 0.7 eV (labeled C). At $T_c = 1$ keV, UL m_a is 3.0 eV, assuming total axion-to-photon conversion (labeled D). To keep UL $m_a > 10^{-6}$ eV, which is the classic axion search lower bound, requires $T_c < 0.1$ MeV (labeled E) or $T_c < 0.4$ MeV with a low axion-to-photon conversion probability of 0.001 (labeled F).

Finally, the normalized axion energy spectrum $dN_a/d\omega$ peaks at $\omega/T_c = 2$ [19]. This implies that the photon energy spectrum would peak at energy T_c. Therefore, for the values of T_c discussed above, in the 1 MeV range or below, the determination of an UL for unpulsed gamma-ray emission in our pulsar sample or preferably younger pulsars with a potentially higher T_c, by future low-energy gamma-ray observatories such as the All-Sky Medium Energy Gamma-Ray Observatory (AMEGO) or e-ASTROGAM, with greater sensitivity than any current observatory in the 0.2–10 MeV band [61,62], may allow an improved determination on the UL m_a presented in this work.

VII. CONCLUSIONS

We analyze data from 17 nearby pulsars using nine years of *Fermi*-LAT data and detect none. Using the UL photon flux and the astrophysical model of Ref. [12], which assumes a pulsar core temperature of 20 MeV, we determine an improved UL axion mass (m_a) of 0.96 and 3.21×10^{-2} eV for axions of energy 100 and 200 MeV respectively. However, we show that at realistic pulsar core temperatures of less than 4 MeV, axion emissivity is so reduced that it is unlikely a reasonable determination of UL m_a can be made with this method. An alternative axion energy loss rate model yields a plausible range of UL m_a values assuming low pulsar core temperatures but requires both the core temperature and the axion-to-photon

conversion probability to be known to set a useful limit. Observation of the unpulsed gamma-ray emission of our selected pulsar sample with future medium-energy gamma-ray observatories such as AMEGO and e-ASTROGAM may allow a better determination of UL m_a.

APPENDIX: NUCLEON PHASE SPACE INTEGRATION

The spin structure function of Eq. (2) has an analytic simplification as presented by Ref. [16], of which we repeat the relevant points here. From the original 12-dimensional integral, seven dimensions may be integrated out analytically so that a five-dimensional integral remains to be solved through numerical integration (as opposed to numerical integration of the four-dimensional integral of Ref. [16]).

First, the three-dimensional momentum delta function is used to integrate out $d^3 p_4$. Then, the nonrelativistic nucleons have energy $E_i = p_i^2 / 2M_N$, and so the energy balance term can be written as:

$$E_1 + E_2 - E_3 - E_4 + \omega$$
$$= \frac{-2p_3^2 - 2\mathbf{p_1} \cdot \mathbf{p_2} + 2\mathbf{p_1} \cdot \mathbf{p_3} + 2\mathbf{p_2} \cdot \mathbf{p_3}}{2M_N} + \omega. \quad \text{(A1)}$$

Next, a polar coordinate system is used, with α and β being the polar and azimuthal angles of $\mathbf{p_2}$ relative to $\mathbf{p_1}$ and θ and Φ being those of $\mathbf{p_3}$. The medium is isotropic, so

the $\mathbf{p_1}$ momentum can be chosen in the z direction so $\int d^3\mathbf{p_1} = 4\pi \int dp_1$ with $p_1 = |\mathbf{p_1}|$. The medium isotropy also allows the azimuthal angle $d\Phi$ to be trivially integrated to leave three nontrivial angular integrations with the remaining angular variables expressed as follows:

$$\mathbf{p_1} \cdot \mathbf{p_2} = p_1 p_2 \cos\alpha \quad \text{(A2)}$$

$$\mathbf{p_1} \cdot \mathbf{p_3} = p_1 p_3 \cos\theta \quad \text{(A3)}$$

$$\mathbf{p_2} \cdot \mathbf{p_3} = p_2 p_3 \cos\alpha \cos\theta + \sin\alpha + \sin\theta + \cos\beta. \quad \text{(A4)}$$

The integration over $d\beta$ is carried out using the δ function with $f(\beta) \equiv E_1 + E_2 - E_3 - E_4 + \omega$ and β_1 being the root of $f(\beta) = 0$ in the interval $[0, \pi]$ giving

$$\int_0^{2\pi} d\beta \delta[f(\beta)] = \frac{2}{|df(\beta)/d\beta|_{\beta=\beta_1}} \Theta\left(\left|\frac{df(\beta)}{d\beta}\right|^2_{\beta=\beta_1}\right). \quad \text{(A5)}$$

The derivative can be expressed as

$$\left|\frac{df(\beta)}{d\beta}\right|_{\beta=\beta_1} = \sqrt{az^2 + bz + c}, \quad \text{(A6)}$$

where

$$z \equiv \cos\alpha \quad \text{(A7)}$$

$$a = p_2^2(-p_1^2 - p_3^2 + 2p_1 p_3 \cos\theta) \quad \text{(A8)}$$

$$b = 2\omega M_N p_1 p_2 - 2p_1 p_2 p_3^2 - 2\omega M_N p_2 p_3 \cos\theta$$
$$+ 2p_1^2 p_3 \cos\theta + 2p_2 p_3^3 \cos\theta - 2p_1 p_2 p_3^2 cos^2\theta \quad \text{(A9)}$$

$$c = \omega^2 M_N^2 + 2\omega M_N p_3^2 + p_2^2 p_3^2 - p_3^4 - 2\omega M_N p_1 p_3 \cos\theta$$
$$+ 2p_1 p_3^3 \cos\theta - p_1^2 p_3^2 cos^2\theta - p_2^2 p_3^2 cos^2\theta. \quad \text{(A10)}$$

Finally, the analytic simplification of Eq. (A5) can be solved by numerical integration through a Monte Carlo method integrating over $dp_1 dp_2 dp_3 d\cos\theta d\cos\alpha$.

[1] R. D. Peccei and H. R. Quinn, CP Conservation in the Presence of Pseudoparticles, Phys. Rev. Lett. **38**, 1440 (1977).

[2] S. Weinberg, A New Light Boson, Phys. Rev. Lett. **40**, 223 (1978).

[3] M. Dine, W. Fischler, and M. Srednicki, A simple solution to the strong *CP* problem with a harmless axion, Phys. Lett. **104B**, 199 (1981).

[4] W. Keil, H.-T. Janka, D. N. Schramm, G. Sigl, M. S. Turner, and J. Ellis, Fresh look at axions and sn 1987a, Phys. Rev. D **56**, 2419 (1997).

[5] G. Rybka, Direct detection searches for axion dark matter, Phys. Dark Universe **4**, 14 (2014).

[6] S. J. Asztalos, G. Carosi, C. Hagmann, D. Kinion, K. van Bibber, M. Hotz, L. J. Rosenberg, G. Rybka, J. Hoskins, J. Hwang, P. Sikivie, D. B. Tanner, R. Bradley, and J. Clarke,

Squid-Based Microwave Cavity Search for Dark-Matter Axions, Phys. Rev. Lett. **104**, 041301 (2010).

[7] L. D. Duffy, P. Sikivie, D. B. Tanner, S. J. Asztalos, C. Hagmann, D. Kinion, L. J. Rosenberg, K. van Bibber, D. B. Yu, and R. F. Bradley, High resolution search for dark-matter axions, Phys. Rev. D **74**, 012006 (2006).

[8] C. Hagmann, D. Kinion, W. Stoeffl, K. van Bibber, E. Daw, H. Peng, L. J. Rosenberg, J. LaVeigne, P. Sikivie, N. S. Sullivan, D. B. Tanner, F. Nezrick, M. S. Turner, D. M. Moltz, J. Powell, and N. A. Golubev, Results from a High-Sensitivity Search for Cosmic Axions, Phys. Rev. Lett. **80**, 2043 (1998).

[9] J. Hoskins, J. Hwang, C. Martin, P. Sikivie, N. S. Sullivan, D. B. Tanner, M. Hotz, L. J. Rosenberg, G. Rybka, A. Wagner, S. J. Asztalos, G. Carosi, C. Hagmann, D. Kinion, K. van Bibber, R. Bradley, and J. Clarke, Search for nonvirialized axionic dark matter, Phys. Rev. D **84**, 121302 (2011).

[10] N. Du *et al.* (ADMX Collaboration), Search for Invisible Axion Dark Matter with the Axion Dark Matter Experiment, Phys. Rev. Lett. **120**, 151301 (2018).

[11] A. Sedrakian, Axion cooling of neutron stars, Phys. Rev. D **93**, 065044 (2016).

[12] B. Berenji, J. Gaskins, and M. Meyer, Constraints on axions and axionlike particles from Fermi large area telescope observations of neutron stars, Phys. Rev. D **93**, 045019 (2016).

[13] N. Iwamoto, Axion Emission from Neutron Stars, Phys. Rev. Lett. **53**, 1198 (1984).

[14] N. Iwamoto, Nucleon-nucleon bremsstrahlung of axions and pseudoscalar particles from neutron-star matter, Phys. Rev. D **64**, 043002 (2001).

[15] C. Hanhart, D. R. Phillips, and S. Reddy, Neutrino and axion emissivities of neutron stars from nucleon-nucleon scattering data, Phys. Lett. B **499**, 9 (2001).

[16] S. Hannestad and G. Raffelt, Supernova neutrino opacity from nucleon-nucleon bremsstrahlung and related processes, Astrophys. J. **507**, 339 (1998).

[17] R. P. Brinkmann and M. S. Turner, Numerical rates for nucleon-nucleon, axion bremsstrahlung, Phys. Rev. D **38**, 2338 (1988).

[18] R. Mayle, J. R. Wilson, J. Ellis, K. Olive, D. N. Schramm, and G. Steigman, Constraints on axions from sn 1987a, Phys. Lett. B **203**, 188 (1988).

[19] G. G. Raffelt, *Stars as Laboratories for Fundamental Physics: The Astrophysics of Neutrinos, Axions, and other Weakly Interacting Particles*, Bibliovault OAI Repository (University of Chicago, Chicago, 1996).

[20] G. G. Raffelt, Astrophysical axion bounds, *Axions: Theory, Cosmology, and Experimental Searches* (Springer-Verlag, Berlin Heidelberg, 2008), Vol. 741, p. 51.

[21] R. N. Manchester, G. B. Hobbs, A. Teoh, and M. Hobbs, The Australia Telescope National Facility Pulsar Catalogue, Astron. J. **129**, 1993 (2005).

[22] A. A. Abdo, M. Ajello, A. Allafort, L. Baldini, J. Ballet, G. Barbiellini, M. G. Baring, D. Bastieri, A. Belfiore, R. Bellazzini, B. Bhattacharyya, E. Bissaldi, E. D. Bloom, E. Bonamente *et al.*, The second Fermi large area telescope catalog of gamma-ray pulsars, Astrophys. J. Suppl. Ser. **208**, 17 (2013).

[23] S. Burke-Spolaor and M. Bailes, The millisecond radio sky: Transients from a blind single-pulse search, Mon. Not. R. Astron. Soc. **402**, 855 (2010).

[24] M. Jiang, B. Y. Cui, N. A. Schmid, M. A. McLaughlin, and Z. C. Cao, Wavelet denoising of radio observations of rotating radio transients (rrats): Improved timing parameters for eight rrats, Astrophys. J. **847**, 13 (2017).

[25] M. Bailes, S. Johnston, J. F. Bell, D. R. Lorimer, B. W. Stappers, R. N. Manchester, A. G. Lyne, L. Nicastro, N. Damico, and B. M. Gaensler, Discovery of four isolated millisecond pulsars, Astrophys. J. **481**, 386 (1997).

[26] D. J. Reardon, G. Hobbs, W. Coles, Y. Levin, M. J. Keith, M. Bailes, N. D. R. Bhat, S. Burke-Spolaor, S. Dai, M. Kerr, P. D. Lasky, R. N. Manchester, S. Oslowski, V. Ravi, R. M. Shannon, W. van Straten, L. Toomey, J. Wang, L. Wen, X. P. You, and X. J. Zhu, Timing analysis for 20 millisecond pulsars in the Parkes pulsar timing array, Mon. Not. R. Astron. Soc. **455**, 1751 (2016).

[27] R. N. Manchester, A. G. Lyne, J. H. Taylor, J. M. Durdin, M. I. Large, and A. G. Little, 2nd Molonglo pulsar survey—discovery of 155 pulsars, Mon. Not. R. Astron. Soc. **185**, 409 (1978).

[28] B. C. Siegman, R. N. Manchester, and J. M. Durdin, Timing parameters for 59 pulsars, Mon. Not. R. Astron. Soc. **262**, 449 (1993).

[29] R. N. Manchester, A. G. Lyne, N. Damico, M. Bailes, S. Johnston, D. R. Lorimer, P. A. Harrison, L. Nicastro, and J. F. Bell, The Parkes southern pulsar survey. 1. observing and data analysis systems and initial results, Mon. Not. R. Astron. Soc. **279**, 1235 (1996).

[30] G. Hobbs, A. G. Lyne, M. Kramer, C. E. Martin, and C. Jordan, Long-term timing observations of 374 pulsars, Mon. Not. R. Astron. Soc. **353**, 1311 (2004).

[31] J. D. Pilkington, A. Hewish, S. J. Bell, and T. W. Cole, Observations of some further pulsed radio sources, Nature (London) **218**, 126 (1968).

[32] T. M. Tauris, L. Nicastro, S. Johnston, R. N. Manchester, M. Bailes, A. G. Lyne, J. Glowacki, D. R. Lorimer, and N. Damico, Discovery of psr j0108 − 1431—the closest known neutron-star, Astrophys. J. **428**, L53 (1994).

[33] Z. Arzoumanian, D. J. Nice, J. H. Taylor, and S. E. Thorsett, Timing behavior of 96 radio pulsars, Astrophys. J. **422**, 671 (1994).

[34] M. I. Large, A. E. Vaughan, and R. Wielebinski, Highly dispersed pulsar and 3 others, Nature (London) **223**, 1249 (1969).

[35] H. Craft, R. Lovelace, and J. Sutton, New pulsar, IAU Circ. **2100**, 1 (1968).

[36] B. A. Jacoby, M. Bailes, S. M. Ord, R. T. Edwards, and S. R. Kulkarni, A large-area survey for radio pulsars at high Galactic latitudes, Astrophys. J. **699**, 2009 (2009).

[37] M. Burgay, B. C. Joshi, N. D'Amico, A. Possenti, A. G. Lyne, R. N. Manchester, M. A. McLaughlin, M. Kramer, F. Camilo, and P. C. C. Freire, The Parkes high-latitude pulsar survey, Mon. Not. R. Astron. Soc. **368**, 283 (2006).

[38] A. E. Vaughan, M. I. Large, and R. Wielebinski, Three new pulsars, Nature (London) **222**, 963 (1969).

[39] T. W. Cole and J. D. Pilkington, Search for pulsating radio sources in declination range +44 degrees delta +90 degrees, Nature (London) **219**, 574 (1968).

[40] F. Camilo, D. J. Nice, and J. H. Taylor, A search for milli-second pulsars at Galactic latitudes −50 degrees < b < −20 degrees, Astrophys. J. **461,** 812 (1996).

[41] F. Camilo and D. J. Nice, Timing parameters of 29 pulsars, Astrophys. J. **445,** 756 (1995).

[42] M. Wood, R. Caputo, E. Charles, M. Di Mauro, J. Magill, and Jeremy Perkins (Fermi-LAT Collaboration), Fermipy: An open-source Python package for analysis of Fermi-LAT Data, *Proc. Sci.*, ICRC2017 (2018) 824.

[43] L. B. Leinson, Axion mass limit from observations of the neutron star in cassiopeia A, J. Cosmol. Astropart. Phys. 08 (2014) 031.

[44] S. B. Ruster, V. Werth, M. Buballa, I. A. Shovkovy, and D. H. Rischke, Phase diagram of neutral quark matter: Self-consistent treatment of quark masses, Phys. Rev. D **72,** 034004 (2005).

[45] H. Shen, H. Toki, K. Oyamatsu, and K. Sumiyoshi, Relativistic equation of state of nuclear matter for supernova and neutron star, Nucl. Phys. **A637,** 435 (1998).

[46] A. Akmal, V. R. Pandharipande, and D. G. Ravenhall, Equation of state of nucleon matter and neutron star structure, Phys. Rev. C **58,** 1804 (1998).

[47] R. Negreiros, V. A. Dexheimer, and S. Schramm, Quark core impact on hybrid star cooling, Phys. Rev. C **85,** 035805 (2012).

[48] M. B. Larson and B. Link, Superfluid friction and late-time thermal evolution of neutron stars, Astrophys. J. **521,** 271 (1999).

[49] G. G. Pavlov, G. S. Stringfellow, and F. A. Cordova, Hubble space telescope observations of isolated pulsars, Astrophys. J. **467,** 370 (1996).

[50] G. G. Pavlov, B. Rangelov, O. Kargaltsev, A. Reisenegger, S. Guillot, and C. Reyes, Old but still warm: Far-uv detection of psr $b0950 + 08$, Astrophys. J. **850,** 79 (2017).

[51] E. H. Gudmundsson, C. J. Pethick, and R. I. Epstein, Neutron star envelopes, Astrophys. J. **259,** L19 (1982).

[52] K. Nomoto and S. Tsuruta, Cooling of neutron-stars—effects of the finite-time scale of thermal conduction, Astrophys. J. **312,** 711 (1987).

[53] D. Yakovlev and C. Pethick, Neutron star cooling, Annu. Rev. Astron. Astrophys. **42,** 169 (2004).

[54] C. O. Heinke and W. C. G. Ho, Direct observation of the cooling of the cassiopeia a neutron star, Astrophys. J. Lett. **719,** L167 (2010).

[55] K. Sumiyoshi, S. Yamada, H. Suzuki, H. Shen, S. Chiba, and H. Toki, Postbounce evolution of core-collapse supernovae: Long-term effects of the equation of state, Astrophys. J. **629,** 922 (2005).

[56] J. A. Pons, S. Reddy, M. Prakash, J. M. Lattimer, and J. A. Miralles, Evolution of proto-neutron stars, Astrophys. J. **513,** 780 (1999).

[57] K. Nakazato, H. Suzuki, and H. Togashi, Heavy nuclei as thermal insulation for protoneutron stars, Phys. Rev. C **97,** 035804 (2018).

[58] L. G. Zhu, J. L. Lu, and L. Wang, Effects of temperature on the structure of neutron stars at high temperature, Gen. Relativ. Gravit. **50,** 11 (2018).

[59] R. Perna, W. C. G. Ho, L. Verde, M. van Adelsberg, and R. Jimenez, Signatures of photon-axion conversion in the thermal spectra and polarization of neutron stars, Astrophys. J. **748,** 116 (2012).

[60] J. F. Fortin and K. Sinha, Constraining axion-like-particles with hard x-ray emission from magnetars, J. High Energy Phys. 18 (2018) 48.

[61] R. Rando, The all-sky medium energy gamma-ray observatory, J. Instrum. **12,** C11024 (2017) .

[62] A. D. Angelis *et al.*, Science with e-astrogam: A space mission for mevgev gamma-ray astrophysics, J. High Energy Astrophys. 19 (**2018**) 1.

[63] M. Wenger, F. Ochsenbein, D. Egret, P. Dubois, F. Bonnarel, S. Borde, F. Genova, G. Jasniewicz, S. Laloë, S. Lesteven, and R. Monier, The SIMBAD astronomical database. The CDS reference database for astronomical objects, Astron. Astrophys. Suppl. Ser. **143,** 9 (2000).